A tissue-like soft all-hydrogel battery

Tingting Ye, Jiacheng Wang, Yiding Jiao, Luhe Li, Er He, Lie Wang, Yiran Li, Yanjing Yun, Dan Li, Jiang Lu, Hao Chen, Qianming Li, Fangyan Li, Rui Gao, Huisheng Peng, Ye Zhang*

T. Ye, J. Wang, Y. Jiao, L. Li, E. He, Dr. L. Wang, Y. Li, Y. Yun, J. Lu, H. Chen, Q. Li, F. Li, R. Gao, Prof. Y. Zhang

National Laboratory of Solid State Microstructures, Jiangsu Key Laboratory of Artificial Functional Materials, Chemistry and Biomedicine Innovation Center (ChemBIC), Collaborative Innovation Center of Advanced Microstructures, College of Engineering and Applied Sciences, Nanjing University, Nanjing 210023, China.

E-mail: yezhang@nju.edu.cn

Dr. D. Li

Department of Immunology, Nanjing University of Chinese Medicine, Nanjing 210046, China.

Prof. H. Peng

State Key Laboratory of Molecular Engineering of Polymers, Department of Macromolecular Science and Laboratory of Advanced Materials, Fudan University, Shanghai 200438, China.

Abstract: To develop wearable and implantable bioelectronics accommodating the dynamic and uneven biological tissues and reducing undesired immune responses, it is critical to adopt batteries with matched mechanical properties with tissues as power sources. However, batteries available cannot reach the softness of tissues due to high Young's moduli of components (*e. g.*, metals, carbon materials, conductive polymers or composite materials). The fabrication of tissue-like soft batteries thus remains a challenge. Here we report the first ultrasoft batteries totally based on hydrogels. The ultrasoft batteries exhibited Young's moduli of 80 kPa, perfectly matching skin and organs (*e. g.*, heart). The high specific capacities of 82 mAh·g^{-1} in all-hydrogel lithium-ion batteries and 370 mAh·g^{-1} in all-hydrogel zinc-ion batteries at a current density of 0.5 A·g^{-1} were achieved. Both high stability and biocompatibility of the all-hydrogel batteries had been demonstrated upon the applications of wearable and implantable. This work illuminates a pathway for designing power sources for wearable and implantable electronics with matched mechanical properties.

1. Introduction

Wearable and implantable bioelectronics are of great significance in the diagnosis, alleviation and treatment of human diseases.[1-5] The power unit is essential for the realization of these functions.[6,7] Due to the advantages of both high energy density and cyclability, batteries are the first choice for the power unit among various energy storage systems.[8,9] The application scenario in wearable and implantable bioelectronics thus requires matched mechanical properties (*e.g.*, Young's moduli) of the batteries with biological tissues.[10-12] On the one hand, it enables stable and close contact with the uneven surface of tissues under dynamic deformations without any mechanical loading, which is beneficial for the continuous and proper functioning of bioelectronics.[13-15] On the other hand, the physical irritation and damage to the tissue can be relieved with matching mechanical properties, thus alleviating the undesirable immune response and health hazard.[16-19] Therefore, it is crucial to design tissue-like soft batteries to develop wearable and implantable bioelectronic devices.

So far, research efforts have been intensively devoted to reducing Young's moduli of the batteries. However, the outcome to date is far from satisfactory.[20-32] The original batteries were based on metal and were intrinsically bulky, rigid and undeformable with Young's moduli of 10^7-10^8 kPa.[21-23] Thin-film batteries were endowed with a certain flexibility, drawing increasing research interests. However, rigid materials such as carbons, conductive polymers, and composites were unavoidable, especially in electrode design. As a result, Young's moduli of these batteries remained too high (10^6-10^8 kPa).[24-27] Although elastic electrodes lately developed from elastomers had reduced Young's moduli of batteries to 10^3-10^5 kPa,[28-31] their rigidity was still magnitudes higher than biological tissues (e.g., skin and organs) with Young's moduli < 10^2 kPa.[33-35] To make the full battery as soft as tissues, it is thus essential to fabricate the battery thoroughly from ultrasoft materials and sacrifice none of their softness in integration.

Here, to the best of our knowledge, tissue-like soft batteries are first reported by all-hydrogel design (**Figure 1**). An integrated battery configuration with superb electrical conductivity and high interface charge transfer efficiency was obtained by taking advantage of the interfacial dry crosslinking strategy. This strategy represents a general and efficient method to achieve ultrasoft batteries with high electrochemical properties. For instance, high specific capacities of 82 mAh·g^{-1} in all-hydrogel lithium-ion batteries and 370 mAh·g^{-1} in all-hydrogel zinc-ion batteries at a current density of 0.5 A·g^{-1} were achieved. Meanwhile, the ultrasoft batteries exhibited Young's moduli of 80 kPa, perfectly matching the mechanical properties of biological tissues. Both high stability and biocompatibility of the all-hydrogel batteries had been demonstrated upon the applications of wearable and implantable.

2. Results and Discussion

As shown in **Figure 2a**, the ultrasoft all-hydrogel battery was obtained by adopting an interfacial dry crosslinking strategy. First, the cathode and anode were made from polyacrylamide (PAM)/carbon nanotube (CNT) hydrogel (**Figure S1**) loaded with active materials. Then, the pristine hydrogel electrodes were fully dehydrated into dehydrated electrodes. Subsequently, rehydration was realized by simply attaching the dehydrated electrodes to the hydrogel electrolytes. Upon contact with the electrolytes, the dehydrated electrodes spontaneously absorbed water from the surface and interior of the electrolytes under combined effects of osmotic pressure and hydrophilic amide groups.[36-38] When reaching rehydration equilibrium, the rehydrated hydrogel electrodes were softened again, and a fused interface was formed between electrode and electrolyte. The all-hydrogel batteries with stable structure and performance were obtained under the isolation of the soft encapsulation layer.

The electrical conductivity of the electrode is one of the critical factors affecting the electrochemical performance of the battery. Poor conductivity of the electrode leads to high internal resistance and consequently low power output. As shown in **Figure 2b**, the electrical conductivities of the pristine hydrogel electrodes were only ~0.8 mS·cm^{-1}. The high water content (~89%) increased the interface resistance of electron transport among CNTs, resulting in poor electrical conductivities. Moreover, the typical sponge-like morphology of the pristine hydrogel electrodes with macropores (sizes of ~20

4

μm) (**Figure 2c**) increased the distance of electrical transfer and further diminished electrical conductivities. Although the pristine hydrogel electrodes possessed low Young's moduli of ~12 kPa, the poor electrical conductivities prevented them from being used in batteries.

When the pristine hydrogel electrodes were fully dehydrated into dehydrated electrodes, the electrical conductivities were improved remarkably to ~2 × 10^3 mS·cm^{-1}. The morphology turned almost non-porous with densified electron pathways (**Figure S2**), leading to increased electrical transfer efficiency. However, the dehydrated electrodes were rigid with high Young's moduli of ~10^8 kPa, which could not meet the requirement of soft batteries.

After the dehydrated electrodes were in contact with the electrolytes and reached rehydration equilibrium, the electrical conductivities of the rehydrated hydrogel electrodes were enhanced to ~10^3 mS·cm^{-1}. To be noted, the weight of water contained in the rehydrated hydrogel electrodes was about 20% of the pristine hydrogel electrodes. Furthermore, the pore size of rehydrated hydrogel electrodes was slightly increased to ~1 μm due to the limited rehydration ratio (**Figure 2d**), preserving the dense electron pathways. The reduced pore sizes of the electrodes during the dehydration process resulted in the high crosslinking density and dense crosslinking network, limiting the water penetration into the hydrogel network.[39,40] The fixed overall water content and osmotic pressure balance further contributed to the ultimate limited water absorption. This limited rehydration ratio was crucial to the high electrical conductivities of the rehydrated hydrogel electrodes. Notably, the rehydrated hydrogel electrodes attached to the hydrogel electrolytes

without electrolyte salt also exhibited high electrical conductivities of ~10^3 mS·cm^{-1} (**Figure S3**), demonstrating that the increase in electrical conductivity was caused by water and structure change rather than the inclusion of electrolyte salt. In addition, the rehydrated hydrogel electrodes exhibited Young's moduli of ~70 kPa, which were well matched with biological tissues. There was generally a restrictive relationship between electrical conductivity and softness of the hydrogel electrode. Considering the bulk resistance and Young's moduli of all-hydrogel batteries based on the rehydrated electrodes with different rehydration ratios, the optimization of the rehydration ratio was investigated. When the rehydration ratio was > 20%, the bulk resistance of the batteries increased dramatically; when the rehydration ratio was < 20%, Young's moduli of the all-hydrogel batteries increased significantly (**Figure S4**). Therefore, a 20% rehydration ratio was selected as a balance.

Besides the intrinsic high electrical conductivities of the electrodes, efficient charge transfer at the electrode-electrolyte interface was also vital for batteries. Charge transfer resistance (R_{ct}) signified the efficiency of electrons shifting across the electrode-electrolyte interface. According to the electrochemical impedance spectroscopy, the R_{ct} of the stacked interface, which was obtained by directly attaching a pristine hydrogel electrode to the electrolyte, was 365 Ω. This electrochemical impedance was much higher than the fused interface (~32 Ω), obtained *via* the interfacial dry crosslinking strategy (**Figure 2e**). The decreased R_{ct} indicated that a compatible interface with high charge transfer was facilitated by interfacial dry crosslinking.

The standard peeling test was used to analyze the interface compatibility (**Figure 2f**). The electrode and electrolyte at the stacked interface were easily peeled off, indicating an incompatible and unstable interface between the pristine hydrogel electrodes and the electrolytes (**Figure S5**). The presence of trace-free water on the surface of the electrolyte reduced the effective interface contact. In addition, the high water content of the system formed a weak boundary layer, which hindered the interaction of the molecular chain at the interface between the electrodes and electrolytes.[41-43]

By contrast, a finger-like pattern was produced at the fused interface upon peeling off. This phenomenon indicated that a higher deformation was required to dissipate energy at the interface after the interfacial dry crosslinking, The adhesion of the electrode-electrolyte interface was greatly enhanced.[42-44] Indeed, the adhesion energy of the fused interface was eight times higher than that of the stacked interface (**Figures 2g** and **S6**). The dehydrated electrode absorbed the trace-free water at the interface through the interfacial dry crosslinking strategy (**Figure S7**), enabling close contact between electrode and electrolyte.[37] The electrode dehydration process reduced the total water content of the system, and the amide groups on the PAM side chains of the electrodes and the electrolytes could form hydrogen bonds at the interface.[47,48] The physical crosslinking of hydrogen bonds enhanced the interface adhesion and stability (**Figure S8**). Moreover, the soft encapsulation layer can effectively prevent the influence of the wet environment on the physical interaction of the interface. After immersion of the battery in deionized water for 24 hours, the interfacial adhesion energy remained at 73 J·m^{-2}, comparable to the interfacial adhesion energy (70 J·m^{-2}) of the battery in air (**Figure S9**). In addition, during the assembly of the all-hydrogel batteries,

the dimensional change rate of the electrodes was mainly reflected in the thickness, and the changes of the plane dimension were almost negligible (**Figure S10**). This dimensional change rule avoids the geometric mismatch between the electrodes and the electrolytes and subsequent deformation and delamination.

Therefore, the ultrasoft hydrogel electrode with excellent electrical conductivity and the hydrogel electrode-electrolyte interface with fast charge transfer efficiency were simultaneously obtained by the interfacial dry crosslinking method. The dehydration process maximized the electrode conductivity for the electrode, and the limited water absorption behavior retained the high conductivity and softness. For the electrode-electrolyte interface, the dehydrated electrode removed trace-free water at the interface to achieve a close contact between the electrode and the electrolyte. Besides, the reduced water content caused the molecular chains in the electrode and the electrolyte to generate hydrogen bonds at the interface, enabling the interface's stable adhesion.

The lithium-ion battery system was used to investigate the electrochemical performances of all-hydrogel batteries. PAM/LiCl hydrogel with ionic conductivity of 8 mS·cm^{-1} was used as the hydrogel electrolyte (**Figure S11**). The cathode and anode were obtained by loading with $LiMn_2O_4$ (LMO) and $LiTi_2(PO_4)_3$ (LTP) (**Figure S12**), respectively. The cyclic voltammograms of rehydrated PAM/CNT-LMO and PAM/CNT-LTP hydrogel electrodes were first tested by three-electrode systems. The characteristic redox peaks revealed that the redox reactions could be reversibly operated (**Figure**

3a). According to the tested capacities, the mass ratio of LMO to LTP was designed to be 1.2:1 in assembly to ensure efficient utilization of materials (**Figures S13** and **S14**). The as-assembled battery exhibited superior electrochemical performance thanks to the improved conductivity and interface. Galvanostatic charge-discharge curves similar to conventional aqueous lithium-ion batteries with an average discharge voltage plateau of 1.5 V were exhibited (**Figure 3b**). The specific discharge capacity was 82 mAh·g^{-1} based on the mass of LTP at a current density of 0.5 A·g^{-1}. As shown in **Figure S15**, promising rate performance of the as-prepared battery was realized, with discharge capacities of 72 mAh·g^{-1} at 0.75 A·g^{-1}, 66 mAh·g^{-1} at 1 A·g^{-1} and 60 mAh·g^{-1} at 1.25 A·g^{-1}. Moreover, the capacity was recovered after being reversed to the initial current density. The all-hydrogel battery also performed high stability, *e.g.*, 65% capacity retention was achieved over 400 cycles at a current density of 1 A·g^{-1} (**Figure 3c**). Besides, the all-hydrogel battery could be charged and discharged typically under the environment with different humidity (**Figure S16**), and the specific discharge capacity and cycle stability were unaffected (**Figure S17**), demonstrating the viability of the all-hydrogel battery in bio-applications. This strategy was also suitable for other all-hydrogel batteries systems. When the active materials were replaced with Zn nanosheet and $NH_4V_4O_{10}$, an all-hydrogel zinc-ion battery with a high discharge capacity of 370 mAh·g^{-1} at a current density of 0.5 A·g^{-1} was obtained (**Figure 3d**) and exhibited 73% capacity retention over 200 cycles at a current density of 2 A·g^{-1} (**Figure 3e**).

Along with the high electrochemical performance, mechanical properties matching perfectly with biological tissues were accomplished for the all-hydrogel batteries (**Figure 4a**). The Young's moduli of electrodes, electrolytes, all-hydrogel batteries and encapsulation layers were calculated based on

the linear segment of the stress-strain curve, which were 70, 8, 80 and 47 kPa, respectively (**Figures 4b** and **S18**). The ultrasoft batteries were compliant to fulfill the attachment to the surface of multiple polyhedrons, exemplifying the stable battery-tissue interface (**Figure 4c**).

The structural integrity and steady interface were also maintained perfectly under dynamic deformations. Due to the adhesiveness of the fused interface and the similar mechanical properties of the components, delamination and dislocation of the electrodes and electrolytes upon deformation were prevented. After 1000 cycles of 180° bending, 30% stretching and 90° twisting, the adhesion energy and shear strength between the electrodes and the electrolytes remained almost unchanged (**Figures 4d**, **S19** and **S20**). Moreover, the impedance of the all-hydrogel battery exhibited minor fluctuations under repeated deformations, proving the steadiness of the interface from the perspective of charge transfer (**Figure 4e**). The integrated battery structure was conducive to the stable power output under deformations. The all-hydrogel batteries exhibited nearly no capacities loss after 5,000 bending cycles at 180° and stretching cycles by 30% (**Figure 4f**). The soft all-hydrogel batteries maintained stable capacities after twisting at 90° for 5,000 cycles and various twisting angles (**Figures 4f** and **S21**). Even under harsh shearing deformation for 5,000 cycles, the capacities remained unaltered (**Figure 4f**), avoiding batteries malfunction caused by external friction. Compared with other flexible batteries based on hydrogels, our all-hydrogel batteries delivered significantly improved flexibility and softness while retaining high electrochemical performance (**Figure S22** and **Table S1**). This structural and electrochemical stability during deformation ensured the proper functioning of the all-hydrogel batteries under dynamic physiological conditions.

Interestingly, a self-healing lithium-ion all-hydrogel battery with similar high electrochemical properties *(e.g.*, the specific discharge capacity of 79 mAh·g^{-1} at a current density of 0.5 A·g^{-1}) could be realized when a second functional component with abundant hydroxyl groups, *e.g.*, agar, was introduced to the hydrogel electrodes. The increasing hydrogen bonds allowed the self-restoration of the electrodes after cutting, and the discharge voltage plateau and capacitance displayed no noticeable decrease (**Figure S23**).

An outlook for the practical application of the all-hydrogel batteries was further provided. As shown in **Figure 5a**, the all-hydrogel battery was closely attached to the wrist and deformed synchronously with the wrist joint, and the stable discharge platform was maintained. The stable cycle performance at 36 ℃proved that the body temperature has no significant effect on the performance of the all-hydrogel battery (**Figure S24**). In practical application, it is essential to avoid the overheat of the bioelectronics. The thermal imaging illustrated that the all-hydrogel battery showed similar temperatures to the skin during the charge and discharge process (**Figure 5b**). Meanwhile, no prominent heat generation was perceived in this progress, preventing possible discomfort or damage to the biological tissues (**Figure 5c**).

Furthermore, the all-hydrogel battery was integrated with a hydrogel strain sensor and attached to the surface of the heart to monitor the heartbeat (**Figure 5d**). Due to the electrostatic and dynamic catechol chemistry interactions between the encapsulation layer and the tissue[49], the all-hydrogel

battery could be stably attached to the heart surface (**Figure S25**). The ultrasoft detection system formed a close and steady contact with the heart, ensuring the accuracy of the signals (**Figure S26**). As shown in **Figure 5e**, the detection system precisely detected the strain change induced by the heartbeat, while no voltage fluctuation of the all-hydrogel battery was observed.

To evaluate the biocompatibility of all-hydrogel batteries, characterizations both *in vitro* and *in vivo* were performed. Take the all-hydrogel lithium-ion battery as an example. After immersion of the all-hydrogel battery in water for 15 days, no significant increase of Li^+ content was detected from the immersing solution, indicating negligible health risk of tissue toxication (**Figure S27**), which was further verified by cytotoxicity experiment *in vitro*. To fully verify the biocompatibility of all-hydrogel batteries with various tissues, three types of cells were selected for the cytotoxicity test, *i.e.*, mouse fibroblasts (L929), mouse skeletal muscle cells (C2C12) and human umbilical vein endothelial cells (HUVEC). All the all-hydrogel battery-conditioned cell culture media had shown comparable cytotoxicity to control after 24 hours of cultures (**Figures S28** and **S29**). Subsequently, all-hydrogel batteries were implanted in mice for 15 and 30 days to explore the safety during long-term usage *in vivo*. The blood indexes of implanted groups exhibited no noticeable differences compared with the controls (**Figure S30**). Moreover, indicators of organ-specific diseases and blood levels of enzymes and electrolytes fell within the confidence intervals of control values (**Figure S31**). Besides, the H&E stained tissue slices of major organs (*e.g.*, heart, liver, spleen, lung and kidney) of implanted groups showed no noticeable pathological changes compared with the controls (**Figures S32** and **5f**), stipulating ensured battery safety *in vivo*. High electrochemical performance and biocompatibility

12

proved the high potentials of all-hydrogel batteries to power wearable and implantable bioelectronics.

3. Conclusion

In summary, we have developed tissue-like soft all-hydrogel batteries *via* an interfacial dry crosslinking strategy. The as-fabricated batteries exhibited desirable high electrochemical properties and tissue-like Young's moduli, offering a practical pathway to tackle the mechanical mismatch between batteries and biological tissues for wearable and implantable bioelectronics. This work also provides a general and promising strategy for developing next-generation energy storage devices and other electronic devices aiming at bio-related applications.

4. Experimental Section

Preparation of PAM/CNT conductive hydrogel: 1 M acrylic amide (AAm), 0.28 wt% (relative to AAm) methylene-bis-acrylamide (MBA) as a crosslinker and 2.8 wt% (relative to AAm) ammonium persulphate (APS) as an initiator were added to 30 wt% carbon nanotube (CNT)/water dispersion and stirred for 1 hour. Subsequently, 0.2 % (relative to solution) N,N,N',N'-

tetramethylethylenediamine (TEMED) as catalyst was added to promote free-radical polymerization. The obtained solution was poured into a petri-dish to form the PAM/CNT conductive hydrogel.

Preparation of hydrogel electrolyte: 2 M AAm, 2 M LiCl and 0.14 wt% (relative to AAm) MBA were dissolved in deionized water under stirring. Meanwhile, argon was pumped into the clear solution to remove oxygen thoroughly. Then, 1.4 wt% (relative to AAm) APS and 0.6% (relative to solution) TEMED were added. Finally, the above solution was transferred into a petri-dish to obtain the PAM/LiCl hydrogel electrolyte. The PAM/zinc trifluoromethanesulfonate (Zn(OTf)$_2$) hydrogel electrolyte for all-hydrogel zinc-ion battery was prepared by immersing the dry PAM film in a 3 M Zn(OTf)$_2$ solution for 24 hours.

Fabrication of all-hydrogel battery: The active material dispersions were firstly added dropwise onto the PAM/CNT conductive hydrogel (area: 1 × 0.5 cm, thickness: 750 µm). The active material dispersion was a mixture of active material (LMO/LTP), super P and PVDF with mass ratios of 16:3:1 in N-methyl-pyrrolidone (NMP) with a concentration of 80 mg·mL^{-1}. The active material dispersion was sonicated for 30 s to realize a uniform dispersion. Then the dispersion was dropped evenly on the surface of the conductive hydrogel using a pipette to obtain the pristine hydrogel electrodes. LMO and LTP mass loadings were 1.2 and 1 mg·cm^{-2}, respectively. Afterward, the pristine hydrogel electrodes were first placed on a hot plate with a temperature of 80 °C to be thoroughly dehydrated and then transferred into a 100 °C vacuum oven for 12 hours to remove NMP. The pristine hydrogel electrodes were placed on the glass plate for dehydration to prevent the electrodes from wrinkling,

owing to the adhesion between the hydrogel electrodes and the glass plate. Then, the hydrogel electrolyte was sandwiched between two dehydrated electrodes. The area of the electrolyte was the same as the electrode, and the thickness was 1 mm. Since the water absorption behavior of the electrode from the electrolyte was spontaneous, it was only necessary to place the sandwich battery in a room temperature environment and wait for the electrodes to reach water absorption equilibrium. After the electrodes were rehydrated to equilibrium (thickness: 450 µm), the integrated all-hydrogel battery was further wrapped by a soft encapsulation layer. The encapsulation layer was prepared by putting a polyacrylic acid-chitosan-tannic acid-Al^{3+} adhesive hydrogel outer layer on the pre-stretch Parafilm inner layer. Parafilm exhibited self-adhesive property under pressure due to the molecular chain shift that increased the intermolecular interactions. Similarly, there were also intermolecular interactions in Parafilm and rehydrated hydrogel electrodes to stabilize the Parafilm-battery interface. The polyacrylic acid-chitosan-tannic acid-Al^{3+} hydrogel was chosen as the outer layer because of its excellent biocompatibility and underwater adhesion to biological tissues, and it was prepared according to the previously reported method.[49] The fabricated of the all-hydrogel zinc-ion battery was with the same method by replacing the active materials with Zn nanosheet and $NH_4V_4O_{10}$.

Supporting Information

Supporting Information is available from the Wiley Online Library or from the author.

Acknowledgments

Conflict of Interest

The authors declare no conflict of interest.

Data Availability Statement

The data that support the findings of this study are available from the corresponding author upon reasonable request.

Keywords: soft, flexible, biocompatible, hydrogel, battery

References

[1]   Z. Li, X. Tian, C.-W. Qiu, J. S. Ho, *Nat. Electron.* **2021**, *4*, 382-391.

[2]   M. Amjadi, S. Sheykhansari, B. J. Nelson, M. Sitti, *Adv. Mater.* **2018**, *30*, 1-19.

[3]   T. Someya, Z. Bao, G. G. Malliaras, *Nature* **2016**, *540*, 379-385.

[4]   R. Chen, A. Canales, P. Anikeeva, *Nat. Rev. Mater.* **2017**, *2*, 1-16.

[5]   G. Courtine, M. V. Sofroniew, *Nat. Med.* **2019**, *25*, 898-908.

[6]   T. R. Ray, J. Choi, A. J. Bandodkar, S. Krishnan, P. Gutruf, L. Tian, R. Ghaffari, J. A. Rogers, *Chem. Rev.* **2019**, *119*, 5461-5533.

[7]   S. Y. Yang, V. Sencadas, S. S. You, N. Z. X. Jia, S. S. Srinivasan, H. W. Huang, A. E. Ahmed, J. Y. Liang, G. Traverso, *Adv. Funct. Mater.* **2021**, 2009289.

[8]   D. C. Bock, A. C. Marschilok, K. J. Takeuchi, E. S. Takeuchi, *Electrochim Acta* **2012**, *84*, 155-164.

[9]   C. Steiger, A. Abramson, P. Nadeau, A. P. Chandrakasan, R. Langer, G. Traverso, *Nat. Rev. Mater.* **2018**, *4*, 83-98.

[10]   J. Kim, R. Ghaffari, D.-H. Kim, *Nat. Biomed. Eng.* **2017**, *1*, 1-4.

[11]   S. I. Park, D. S. Brenner, G. Shin, C. D. Morgan, B. A. Copits, H. U. Chung, M. Y. Pullen, K. N. Noh, S. Davidson, S. J. Oh, J. Yoon, K.-I. Jang, V. K. Samineni, M. Norman, J. G. Grajales-Reyes, S. K. Vogt, S. S. Sundaram, K. M. Wilson, J. S. Ha, R. Xu, T. Pan, T.-I. Kim, Y. Huang, M. C. Montana, J. P. Golden, M. R. Bruchas, R. W. Gereau, J. A. Rogers, *Nat. Biotechnol.* **2015**, *33*, 1280-1286.

[12]   H. Ouyang, Z. Liu, N. Li, B. Shi, Y. Zou, F. Xie, Y. Ma, Z. Li, H. Li, Q. Zheng, X. Qu, Y. Fan, Z. L. Wang, H. Zhang, Z. Li, *Nat. Commun.* **2019**, *10*, 1-10.

[13]   K. Sim, F. Ershad, Y. Zhang, P. Yang, H. Shim, Z. Rao, Y. Lu, A. Thukral, A. Elgalad, Y. Xi, B. Tian,
         D. A. Taylor, C. Yu, *Nat. Electron.* **2020**, *3*, 775-784.

[14]   J. Deng, H. Yuk, J. Wu, C. E. Varela, X. Chen, E. T. Roche, C. F. Guo, X. Zhao, *Nat. Mater.* **2021**,
         20, 229-236.

[15]   S. Xu, Y. Zhang, L. Jia, K. E. Mathewson, K.-I. Jang, J. Kim, H. Fu, X. Huang, P. Chava, R. Wang,
         S. Bhole, L. Wang, Y. J. Na, Y. Guan, M. Flavin, Z. Han, Y. Huang, J. A. Rogers, *Science* **2014**,
         344, 70-74.

[16]   I. R. Minev, P. Musienko, A. Hirsch, Q. Barraud, N. Wenger, E. M. Moraud, J. Gandar, M.
         Capogrosso, T. Milekovic, L. Asboth, R. F. Torres, N. Vachicouras, Q. Liu, N. Pavlova, S. Duis,
         A. Larmagnac, J. Vörös, S. Micera, Z. Suo, G. Courtine, S. P. Lacour, *Science* **2015**, *347*, 159-
         163.

[17]   R. Feiner, T. Dvir, *Nat. Rev. Mater.* **2017**, *3*, 1-16.

[18]   Y. Liu, J. Liu, S. Chen, T. Lei, Y. Kim, S. Niu, H. Wang, X. Wang, A. M. Foudeh, J. B. Tok, Z. Bao,
         Nat. Biomed. Eng. **2019**, *3*, 58-68.

[19]   J. W. Salatino, K. A. Ludwig, T. D. Y. Kozai, E. K. Purcell, *Nat. Biomed. Eng.* **2017**, *1*, 862-877.

[20]   H. R. Lim, H. S. Kim, R. Qazi, Y. T. Kwon, J. W. Jeong, W. H. Yeo, *Adv. Mater.* **2020**, *32*,
         e1901924.

[21]   D. J. Young, P. Cong, M. A. Suster, M. Damaser, *Lab Chip* **2015**, *15*, 4338-4347.

WILEY-VCH

[22]   X. Huang, D. Wang, Z. Yuan, W. Xie, Y. Wu, R. Li, Y. Zhao, D. Luo, L. Cen, B. Chen, H. Wu, H. Xu, X. Sheng, M. Zhang, L. Zhao, L. Yin, *Small* **2018**, *14*, e1800994.

[23]   M. Mimee, P. Nadeau, A. Hayward, S. Carim, S. Flanagan, L. Jerger, J. Collins, S. McDonnell, R. Swartwout, R. J. Citorik, l. Bulović, R. Langer, G. Traverso, A. P. Chandrakasan, T. K. Lu, *Science* **2018**, *360*, 915-918.

[24]   L. Hu, H. Wu, F. L. Mantia, Y. Yang, Y. Cui, *ACS Nano* **2010**, *4*, 5843-5848.

[25]   H. Li, C. Han, Y. Huang, Y. Huang, M. Zhu, Z. Pei, Q. Xue, Z. Wang, Z. Liu, Z. Tang, Y. Wang, F. Kang, B. Li, C. Zhi, *Energy Environ. Sci.* **2018**, *11*, 941-951.

[26]   J. Wan, J. Xie, X. Kong, Z. Liu, K. Liu, F. Shi, A. Pei, H. Chen, W. Chen, J. Chen, X. Zhang, L. Zong, J. Wang, L. Q. Chen, J. Qin, Y. Cui, *Nat. Nanotechnol.* **2019**, *14*, 705-711.

[27]   A. J. Bandodkar, S. P. Lee, I. Huang, W. Li, S. Wang, C. J. Su, W. J. Jeang, T. Hang, S. Mehta, N. Nyberg, P. Gutruf, J. Choi, J. Koo, J. T. Reeder, R. Tseng, R. Ghaffari, J. A. Rogers, *Nat. Electron.* **2020**, *3*, 554-562.

[28]   W. Weng, Q. Sun, Y. Zhang, S. He, Q. Wu, J. Deng, X. Fang, G. Guan, J. Ren, H. Peng, *Adv. Mater.* **2015**, *27*, 1363-1369.

[29]   M. Gu, W.-J. Song, J. Hong, S. Y. Kim, Tae Joo Shin5, N. A. Kotov, S. Park, B.-S. Kim, *Sci. Adv.* **2019**, *5*, eaaw1879.

[30]   X. Chen, H. Huang, L. Pan, T. Liu, M. Niederberger, *Adv. Mater.* **2019**, *31*, e1904648.

[31] D. G. Mackanic, X. Yan, Q. Zhang, N. Matsuhisa, Z. Yu, Y. Jiang, T. Manika, J. Lopez, H. Yan, K. Liu, X. Chen, Y. Cui, Z. Bao, *Nat. Commun.* **2019**, *10*, 1-11.

[32] Y. Guo, J. Bae, Z. Fang, P. Li, F. Zhao, G. Yu, *Chem. Rev.* **2020**, *120*, 7642-7707.

[33] Y. Ohm, C. Pan, M. J. Ford, X. Huang, J. Liao, C. Majidi, *Nat. Electron.* **2021**, *4*, 185-192.

[34] S. P. Lacour, G. Courtine, J. Guck, *Nat. Rev. Mater.* **2016**, *1*, 1-14.

[35] C. F. Guimarães, L. Gasperini, A. P. Marques, R. L. Reis, *Nat. Rev. Mater.* **2020**, *5*, 351-370.

[36] R. Michel, L. Poirier, Q. van Poelvoorde, J. Legagneux, M. Manassero, L. Corte, *Proc. Natl. Acad. Sci. U. S. A.* **2019**, *116*, 738-743.

[37] H. Yuk, C. E. Varela, C. S. Nabzdyk, X. Mao, R. F. Padera, E. T. Roche, X. Zhao, *Nature* **2019**, *575*, 169-174.

[38] L. Zhang, J. B. Bailey, R. H. Subramanian, A. Groisman, F. A. Tezcan, *Nature* **2018**, *557*, 86-91.

[39] G. Chen, G. Wang, X. Tan, K. Hou, Q. Meng, P. Zhao, S. Wang, J. Zhang, Z. Zhou, T. Chen, Y. Cheng, B. S. Hsiao, E. Reichmanis, M. Zhu, *Natl. Sci. Rev.* **2020**, *0*, 1-12.

[40] T. Chen, P. Wei, G. Chen, H. Liu, I. T. Mugaanire, K. Hou, M. Zhu, *J. Mater. Chem. A.* **2021**, *9*, 12265-12275.

[41] W. Zhang, R. Wang, Z. Sun, X. Zhu, Q. Zhao, T. Zhang, A. Cholewinski, F. K. Yang, B. Zhao, R. Pinnaratip, P. K. Forooshani, B. P. Lee, *Chem. Soc. Rev.* **2020**, *49*, 433-464.

[42] F. Pan, S. Ye, R. Wang, W. She, J. Liu, Z. Sun, W. Zhang, *Mater. Horiz.* **2020**, *7*, 2063-2070.

20

[43]   C. Cui, T. Wu, F. Gao, C. Fan, Z. Xu, H. Wang, B. Liu, W. Liu, *Adv. Funct. Mater.* **2018**, *28*, 1-12.

[44]   D. Wirthl, R. Pichler, M. Drack, G. Kettlguber, R. Moser, R. Gerstmayr, F. Hartmann, E. Bradt, R. Kaltseis, C. M. Siket, S. E. Schausberger, S. Hild, S. Bauer, M. Kaltenbrunner, *Sci. Adv.* **2017**, *3*, e1700053.

[45]   H. Yuk, T. Zhang, S. Lin, G. A. Parada, X. Zhao, *Nat. Mater.* **2016**, *15*, 190-196.

[46]   Y. S. Zhang, A. Khademhosseini, *Science* **2017**, *356*, 1-10.

[47]   N. Tanaka, K. Ito, H. Kitano, *Macromolecules* **1994**, *27*, 540-544.

[48]   E. Patyukova, T. Rottreau, R. Evans, P. D. Topham, M. J. Greenall, *Macromolecules* **2018**, *51*, 7032-7043.

[49]   X. Su, Y. Luo, Z. Tian, Z. Yuan, Y. Han, R. Dong, L. Xu, Y. Feng, X. Liu, J. Huang, *Mater. Horiz.* **2020**, *7*, 2651-2661.
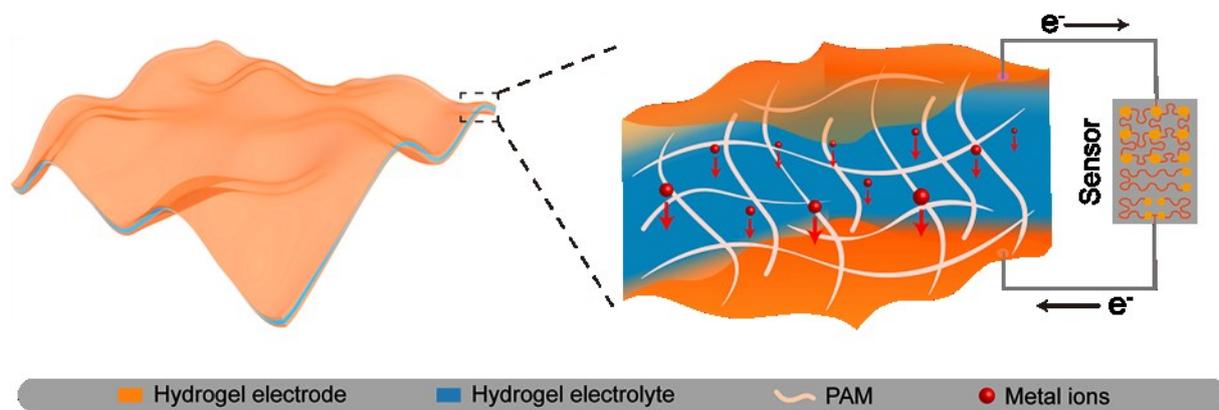
**Figure 1.** Schematic illustration of the structure and working mechanism of the all-hydrogel battery.
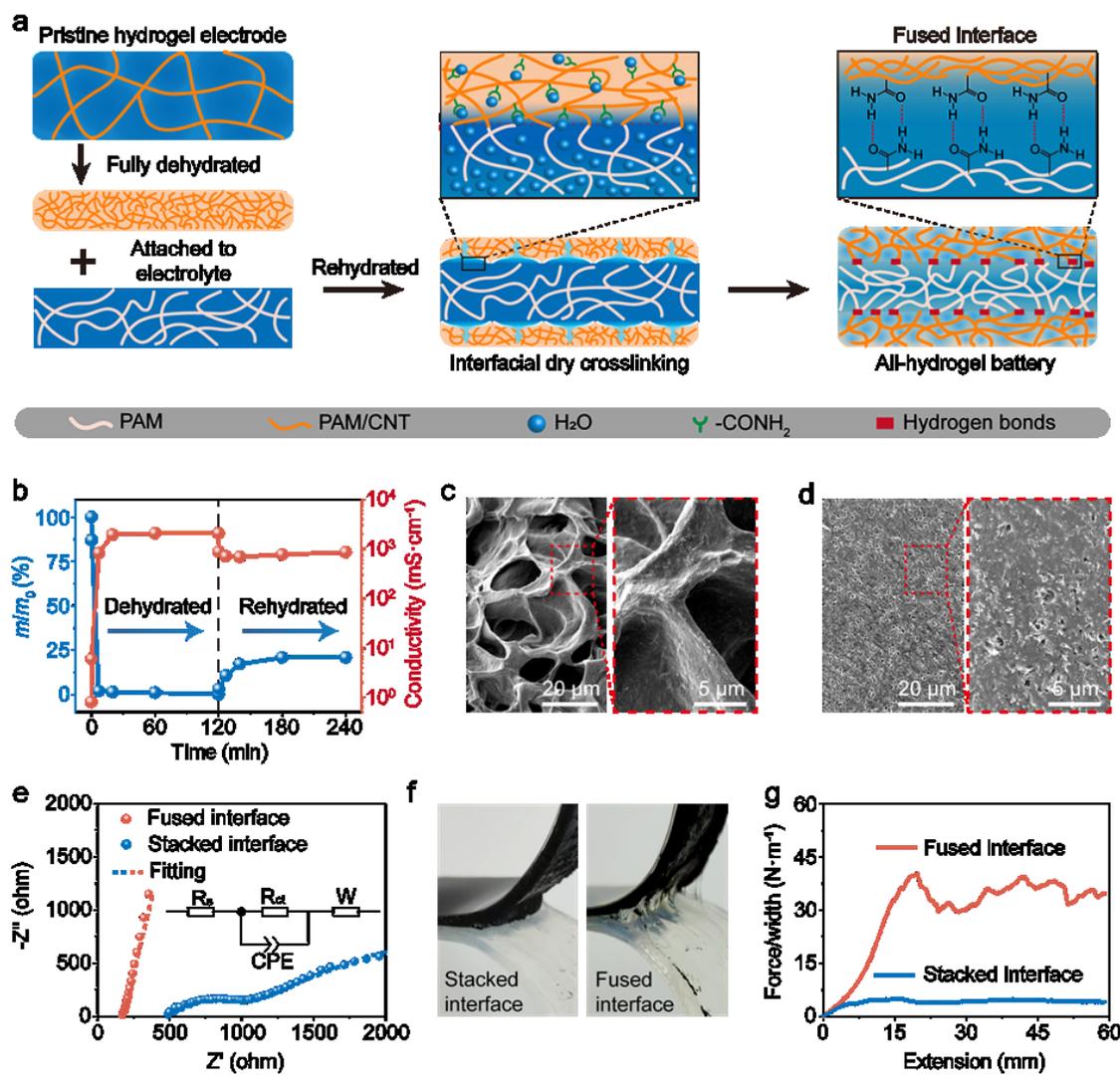
Figure 2. Fabrication and structure characterization of all-hydrogel batteries. a) The preparation process of the all-hydrogel battery through interfacial dry crosslinking. b) Changes in the weight of water and electrical conductivity of hydrogel electrodes during dehydration and rehydration. Here m_0 corresponds to the weight of water in the pristine hydrogel electrode, and m corresponds to the weight of water in the electrode during dehydration and rehydration. c) SEM images of pristine hydrogel electrode. d) Scanning electron microscopy images of rehydrated hydrogel electrode. e)

Electrochemical impedance spectroscopy of all-hydrogel batteries (inset, equivalent circuit). f) Photographs to peel off hydrogel electrode from electrolyte for stacked and fused interfaces. g) Adhesion curves between hydrogel electrode and electrolyte for fused and stacked interfaces.
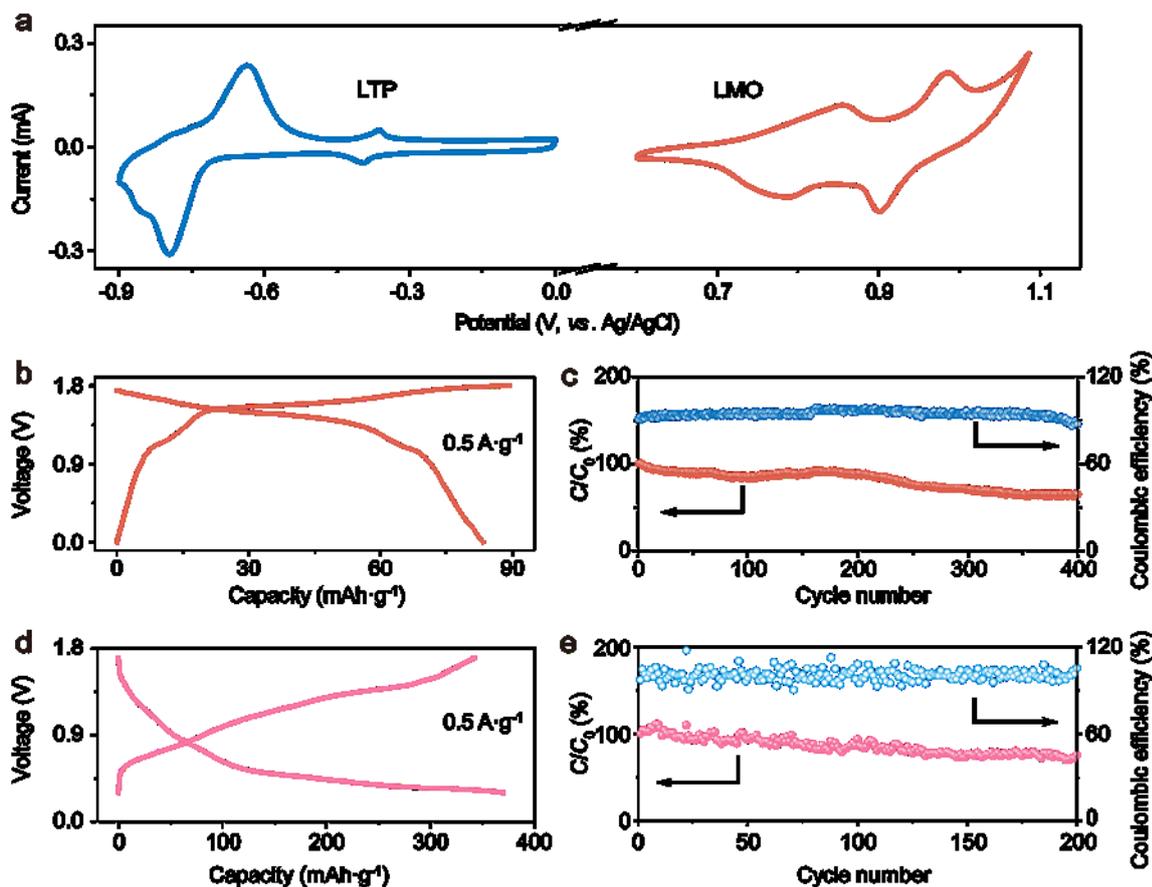

Figure 3. Electrochemical properties of the all-hydrogel batteries. a) Cyclic voltammograms of the rehydrated PAM/CNT-LTP and PAM/CNT-LMO hydrogel electrodes at a scan rate of 0.1 mV·s^{-1}. b) Galvanostatic charge-discharge curve of all-hydrogel lithium-ion battery at a current density of 0.5 A·g^{-1}. c) Cyclic performance of all-hydrogel lithium-ion battery at a current density of 1 A·g^{-1}. Here C_0 and C correspond to the specific capacities before and after the cycle, respectively. d) Galvanostatic charge-discharge curve of all-hydrogel zinc-ion battery at a current density of 0.5 A·g^{-1}. e) Cyclic

performance of all-hydrogel zinc-ion battery at a current density of 2 A·g^{-1}. Here C_0 and C correspond

to the specific capacities before and after the cycle, respectively.
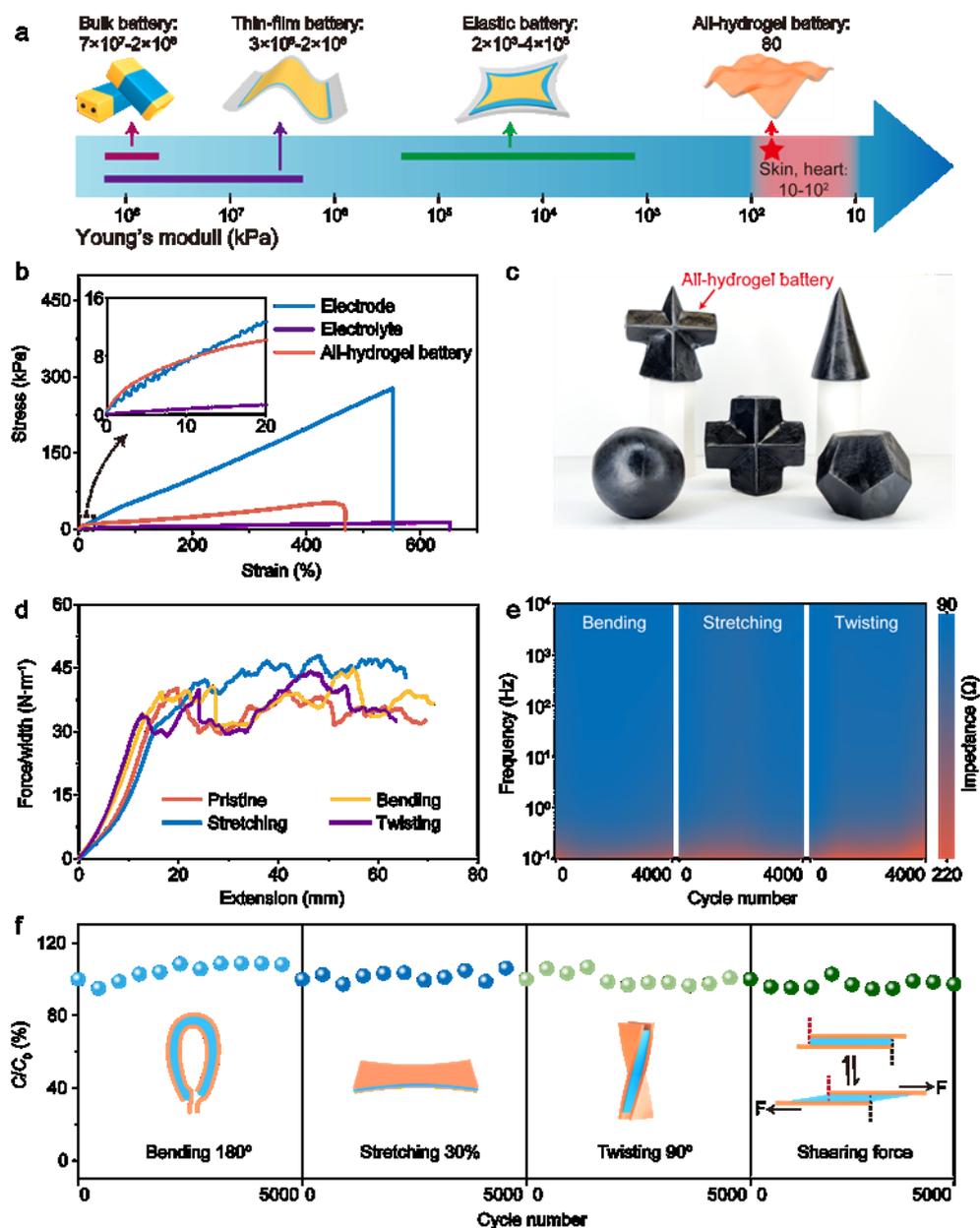
Figure 4. Mechanical properties of the all-hydrogel batteries. a) Comparison of Young's moduli for

all-hydrogel batteries, previous batteries and biological tissues. b) Stress-strain curves of rehydrated

hydrogel electrode, hydrogel electrolyte and all-hydrogel battery (inset, stress-strain curves for strains within 20%). c) Photographs of the all-hydrogel battery attached to surfaces of multiple polyhedrons. The arrow shows the all-hydrogen battery. d) Adhesion curves of the battery interface before and after different deformations with each for 1,000 cycles. e) Impedance of all-hydrogel batteries at different deformation cycles. f) Specific capacitance retention of all-hydrogel batteries after bending, stretching, twisting, and shearing each for 5,000 cycles. Here C_0 and C correspond to the specific capacities before and after deformations, respectively.
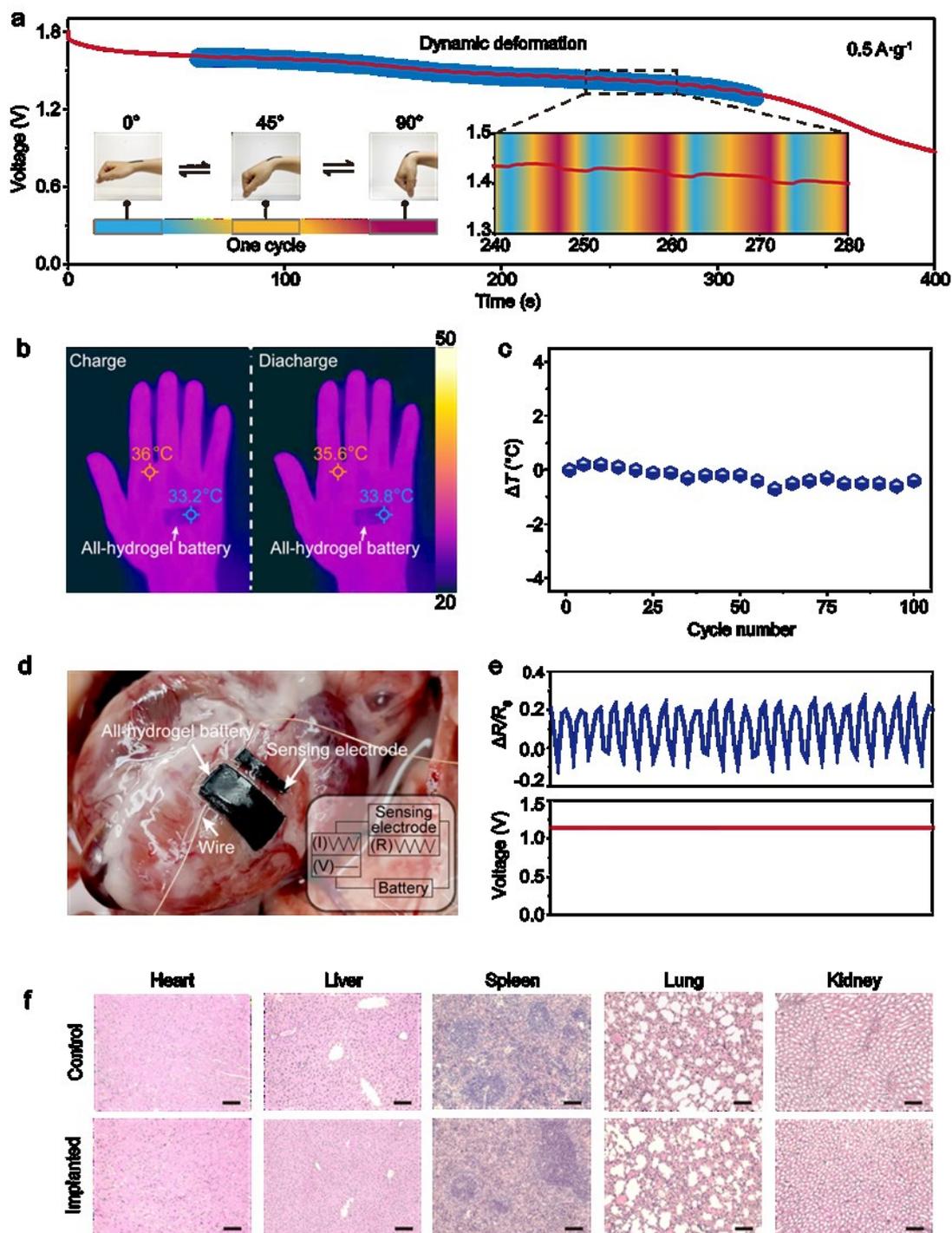
Figure 5. Application of the all-hydrogel batteries. a) Discharge curve at the current density of 0.5 A·g⁻¹ under dynamic deformation of the wrist (left inset, photographs of the wrist attached with an

all-hydrogel battery during bending, and different colors of the bottom ribbon represent different deformation states; right inset, amplification of the discharge curve from 240 to 280 seconds). b) Comparison of thermal imaging of all-hydrogel battery and hand during charging and discharging. c) Temperature variation of all-hydrogel batteries during 100 charge-discharge cycles. d) Detection system with power supply and sensor attached to the surface of the heart (inset, working diagram). e) Variation of the relative resistance of the sensor and voltage of the all-hydrogel battery under heart beating. Here R_0 represents the original resistance before deformation, while ΔR represents the resistance difference before and after deformation. f) The histological data (representative H&E stained sections) of the major organs, including heart, liver, spleen, lung and kidney of control and implanted group for 30 days (scale bar: 100 µm, n = 5).

The Table of Contents

A tissue-like soft all-hydrogel battery

All-hydrogel batteries with Young's moduli of 80 kPa are designed to match the mechanical properties of skin and heart. It exhibits a high specific capacity of 370 mAh·g^{-1} and maintains stability during dynamic deformation. High stability and biocompatibility are realized on the skin and *in vivo*, so the all-hydrogel battery is an ideal power supply for wearable and implantable bioelectronics.